

# Fast collisional $\sqrt{\text{SWAP}}$ gate for fermionic atoms in an optical superlattice

Rafi Weill,<sup>1</sup> Jonathan Nemirovsky,<sup>1</sup> and Yoav Sagi<sup>1,\*</sup>

<sup>1</sup>*Physics Department and Solid State Institute, Technion - Israel Institute of Technology, Haifa 32000, Israel*

(Dated: December 30, 2025)

Collisional gates in optical superlattices have recently achieved record fidelities, but their operation times are typically limited by tunneling. Here we propose and analyze an alternative route to a fast  $\sqrt{\text{SWAP}}$  gate for two fermionic atoms in an optical superlattice based on optimized, time-dependent control of the short and long lattice depths. The gate is implemented by transiently releasing the atoms into a quasi-harmonic confinement centered between the two sites. With an appropriately chosen contact interaction strength, a controlled collision accumulates the exchange phase required for  $\sqrt{\text{SWAP}}$  and generates entanglement. We employ a continuum, time-dependent Schrödinger-equation simulation that goes beyond a two-site Fermi–Hubbard description and benchmark it against experimentally implemented tunneling-based protocols, reproducing the observed single-particle tunneling and spin-exchange dynamics. For experimentally accessible lattice depths, we find that the proposed gate operates in  $\sim 21\ \mu\text{s}$ , more than an order of magnitude faster than tunneling-based implementations, while achieving fidelities  $\gtrsim 99\%$ . We further analyze sensitivity to lattice-depth variations and show that a composite sequence improves robustness. Our results establish fast, collision-mediated entangling gates in superlattices as a promising building block for scalable neutral-atom quantum computation.

## I. INTRODUCTION

Numerical methods that harness the intrinsic quantum properties of physical systems are expected to offer advantages over classical computation in a range of applications, including optimization [1–3], cryptography [4, 5], complex material simulations [6–8], and machine learning [9–11]. In particular, quantum simulations of electronic structures and strongly correlated fermionic phases represent one of the most promising frontiers for demonstrating quantum advantage [12–14]. While such fermionic models can, in principle, be simulated on a universal quantum computer, the required overhead is substantial [12, 15]. An alternative approach is offered by fermionic quantum processors, which provide a more natural framework by directly encoding antisymmetry and particle statistics.

Neutral atoms confined in optical potentials have established themselves as a prominent hardware platform for quantum simulation and computation [16]. Two main architectures are currently being pursued: movable tweezer arrays, which enable flexible, reconfigurable geometries [13, 17–21], and optical lattices, which provide large-scale, highly ordered registers [22–26]. Their key advantages include long coherence times, inherent scalability, and the ability to realize strong, tunable interactions. Substantial progress has been achieved through the use of Rydberg interactions, enabling fast and high-fidelity two-qubit gate operations [27–30]. In this approach, each qubit is localized in an individual trap, with gate interactions mediated by long-range dipole–dipole coupling. These gates operate on microsecond timescales and are relatively insensitive to the thermal motion of

the atoms. Nonetheless, they rely on complex optical excitation schemes to access the Rydberg manifold, and their fidelities are ultimately limited by spontaneous decay from Rydberg or intermediate states.

An alternative approach, known as collisional gates, achieves entanglement in spin and orbital degrees of freedom through controlled atomic motion and contact interactions [31–36]. Recent experiments have demonstrated collisional entangling gates with fidelities approaching 99.75% and Bell-state lifetimes exceeding 10 seconds, achieved through coherent manipulation of fermionic atoms in an optical superlattice [26]. A central mechanism is the composite pair-exchange operation, which relies on the exchange blockade: the symmetry of the two-particle wave function, together with on-site interactions, gives rise to spin entanglement when tunneling is enabled between neighboring sites. The gate duration is primarily determined by the tunneling rate, which depends on the inter-site barrier height controlled by the lattice depth. Adjusting the barrier allows tunneling to be effectively switched on and off. Achieving high fidelity requires minimizing motional excitations during these ramps. While strictly adiabatic changes suppress such excitations, they lead to slower gates and limit circuit-level performance [37]. In practice, shaped pulses of quasi-adiabatic nature have been shown to provide a compromise between speed and fidelity [26].

Here, we present an alternative route to implementing a fast and robust  $\sqrt{\text{SWAP}}$  gate for atoms interacting via contact-like potentials in an optical superlattice. The concept builds on our previous work in a tweezer-based architecture [36], where the strategy was to switch off the individual tweezers while simultaneously turning on an auxiliary harmonic well centered between them. In this configuration, the atomic wave packets evolve as squeezed coherent states and are subsequently recaptured when the tweezers are restored. The key advantage of

\* Electronic address: yoavsagi@technion.ac.il

that approach is that the gate timescale is determined by the harmonic confinement, allowing operations much faster than those limited by tunneling. In a lattice-based setting, however, one cannot directly engineer a perfectly harmonic well; the potential must remain a superlattice [38] at all times,

$$V(x, \tau) = V_S(\tau) \cos^2\left(\frac{\pi x}{a_x}\right) + V_L(\tau) \sin^2\left(\frac{\pi x}{2a_x}\right), \quad (1)$$

where  $V_S$  and  $V_L$  denote the short- and long-lattice depths, respectively, and  $a_x$  is the short-lattice constant.

A straightforward extension of our previous approach would be to completely turn off the short lattice, allow the atoms to evolve for approximately a single transit time, and then restore it. This strategy, however, proves ineffective: the residual long-lattice potential is strongly anharmonic, causing the wave function to disperse into higher bands and leading to a rapid loss of fidelity. In contrast, we demonstrate that retaining a modest short-lattice amplitude yields a quasi-harmonic confinement, and that carefully engineered time-dependent profiles of  $V_S(\tau)$  and  $V_L(\tau)$  can support high-fidelity dynamics while still allowing for fast gate operation.

The remainder of this paper is structured as follows. In Sec. II, we review the analytical intuition developed in our previous tweezer-based protocol and its underlying single-well harmonic dynamics. In Sec. III, we benchmark and validate a continuum numerical simulation against tunneling-based gate sequences from Ref. [26], reproducing key experimental observables. In Sec. IV, we demonstrate near-ideal SWAP gate in a superlattice using optimized control of  $(V_S, V_L)$ . The main result of this work, a fast two-qubit  $\sqrt{\text{SWAP}}$  gate in a superlattice, is presented in Sec. V, where we also analyze its fidelity and robustness. We conclude in Sec. VI with a discussion of the implications and outlook.

## II. FAST COLLISIONAL GATE IN OPTICAL TWEEZERS

In this section we give a short summary of our previous work [36], where we proposed a two-atom gate protocol based on switching two micro-traps into a central harmonic trap. After half a trap period, the system is restored to the initial trap configuration. When the two atoms are non-interacting, this sequence acts as a SWAP gate. With tunable contact interactions, the colliding atoms accumulate a relative  $\pi/2$  phase shift between even and odd components of the wave-function, thereby realizing an entangling  $\sqrt{\text{SWAP}}$  gate.

The dynamics in the central harmonic trap are governed by the time-dependent Schrödinger equation for

two particles [39]:

$$i\hbar \frac{\partial \psi_{ss'}}{\partial \tau} = \left[ -\frac{\hbar^2}{2m} (\nabla_{x_1}^2 + \nabla_{x_2}^2) + V_{\text{ext}}(x_1) + V_{\text{ext}}(x_2) + (1 - \delta_s^s) \gamma \delta_{\text{reg}}(x_1 - x_2) \right] \psi_{ss'} \quad (2)$$

where  $V_{\text{ext}}(x) = \frac{1}{2} m \omega_0^2 x^2$  is the harmonic potential, and  $\gamma$  is the interaction coupling constant governed by a magnetic field near the Feshbach resonance [40]. Changing to center-of-mass,  $X = (x_1 + x_2)/\sqrt{2}$ , and relative,  $x = (x_1 - x_2)/\sqrt{2}$ , coordinates decouples the problem:  $\psi(X, x, \tau) = \psi_0(X, \tau) \psi_1(x, \tau)$ . At  $\tau_{\text{gate}} = \pi/\omega_0$ , the  $\psi_0$  part returns to its initial state, and the gate operation is determined entirely by  $\psi_1(x, \tau)$ .

In the non-interacting case ( $\gamma = 0$ ), the solutions for two wave packets separated by distance  $d$  are displaced squeezed states,

$$\varphi_{\pm}(x, \tau) = \left( \frac{A(\tau)}{\sqrt{\pi}} \right)^{1/2} e^{-i\Theta(\tau)/2} e^{-\frac{|x \pm x_c(\tau)|^2}{\sigma(\tau)^2}} e^{\pm i p_c(\tau) x / \hbar}, \quad (3)$$

with parameters

$$\begin{aligned} A(\tau) &= \sqrt{\frac{m\omega_0}{\hbar}} \frac{1}{\sqrt{\cosh(2r) + \sinh(2r) \cos(2\omega_0\tau)}} \\ \sigma(\tau)^2 &= \frac{2\hbar}{m\omega_0} \left[ \frac{1 + \tanh(r) e^{-2i\omega_0\tau}}{1 - \tanh(r) e^{-2i\omega_0\tau}} \right] \\ e^{-i\Theta(\tau)} &= \left[ \frac{1 + \tanh(r) e^{+2i\omega_0\tau}}{1 + \tanh(r) e^{-2i\omega_0\tau}} \right]^{1/2} e^{-i\omega_0\tau} \\ x_c(\tau) &= \frac{d}{\sqrt{2}} \cos(\omega_0\tau) \\ p_c(\tau) &= m\dot{x}_c(\tau) = -\frac{m\omega_0 d}{\sqrt{2}} \sin(\omega_0\tau) \end{aligned} \quad (4)$$

The squeezing parameter,  $r$ , is determined by the initial condition  $\sigma(0) = \sigma_0$ ,

$$r = \ln \left[ \frac{\sigma_0}{\sqrt{2} \sqrt{\hbar/m\omega_0}} \right]. \quad (5)$$

When interactions are included, the colliding wave-packets scatter with the delta potential at  $x = 0$  and the solution can be expressed as

$$\psi_1(x, \tau) = \begin{cases} \varphi_+(x, \tau) + R \varphi_-(x, \tau), & x > 0 \\ T \varphi_+(x, \tau), & x < 0, \end{cases} \quad (6)$$

with the reflection and transmission coefficients,  $R$  and  $T$ , fixed by continuity and boundary conditions. A  $\sqrt{\text{SWAP}}$  operation requires  $R/T = \pm i$ , which sets condition on  $\gamma$  and  $\tanh(r)$ .

The performance of the  $\sqrt{\text{SWAP}}$  gate is determined by the fidelity:

$$\mathcal{F} = \left| \langle \psi(x_1, x_2, \tau_{\text{gate}}) | \frac{1}{\sqrt{2}} [w_R(x_1) w_L(x_2) + i w_L(x_1) w_R(x_2)] \rangle \right|^2. \quad (7)$$

where  $w_L(x)$  and  $w_R(x)$  are the localized orbitals centered in the left and right wells, respectively.

Numerical simulations of Eq. 2 using the beam propagation method (BPM) [41] showed that this gate sequence can lead to fidelities close to 1, in various experimental settings.

### III. VERIFICATION OF THE NUMERICAL SIMULATION

Before presenting our gate sequence in an optical lattice, we first analyze the gate protocols reported in Ref. [26]. This comparison serves both to benchmark our numerical simulations and to highlight the advantages of the present scheme.

In Ref. [26], Bojović *et al.* demonstrated high-fidelity collisional gates with two fermionic  ${}^6\text{Li}$  atoms confined in an optical superlattice (with short lattice constant  $a_x = 1.14 \mu\text{m}$ ). The experiment realizes isolated double-well potentials formed by superimposing long and short optical lattices, where each double well hosts two atoms. For atoms with parallel spins, the dynamics is frozen due to the suppression of  $s$ -wave interactions by the Pauli principle; we therefore restrict our discussion to the case of opposite spins. The relevant dynamics are captured by the two-site Fermi–Hubbard Hamiltonian,

$$\hat{H}_{\text{FH}} = -t \sum_{\sigma} (\hat{c}_{L,\sigma}^\dagger \hat{c}_{R,\sigma} + \text{h.c.}) + U \sum_{i=L,R} \hat{n}_{i,\uparrow} \hat{n}_{i,\downarrow} + \frac{\delta}{2} \sum_{\sigma} (\hat{n}_{R,\sigma} - \hat{n}_{L,\sigma}) + \Delta_B (\hat{n}_{R,\uparrow} - \hat{n}_{R,\downarrow}), \quad (8)$$

where  $t$  is the tunneling matrix element,  $U$  the on-site interaction,  $\delta$  the spin-independent energy bias between wells, and  $\Delta_B$  a spin-dependent offset. The main experimental knobs are the lattice depths (controlling  $t$  and  $U$ ), the phase between long and short lattices (setting  $\delta$ ), and the magnetic field gradient (tuning  $\Delta_B$ ). The system can be initialized at will in any of the four basis states  $|\uparrow, \downarrow\rangle$ ,  $|\downarrow, \uparrow\rangle$ ,  $|\uparrow\downarrow, 0\rangle$ , or  $|0, \uparrow\downarrow\rangle$ , by applying controlled magnetic-field gradients and adjustable energy tilts between the wells.

While the tight-binding description suffices to analyze the gate sequences proposed in Ref. [26], our protocol involves time dependences and parameter regimes that cannot be captured reliably by a two-site model alone. We therefore simulate the continuum, time-dependent Schrödinger equation for one or two particles (Eq. 2).

In the tight-binding regime, relevant for comparison to Ref. [26], the continuum parameters  $(V, \gamma)$  map onto the Hubbard parameters  $(t, U)$  via Wannier-like localized orbitals  $w_L(x)$  and  $w_R(x)$  centered in the left and right wells of a symmetric double well:

$$U = \gamma \int dx |w_L(x)|^4, \quad (9)$$

$$t = - \int dx w_L^*(x) \left( -\frac{\hbar^2}{2m} \nabla^2 + V(x) \right) w_R(x). \quad (10)$$

We obtain  $w_L(x)$  and  $w_R(x)$  by diagonalizing the single-particle Hamiltonian of an isolated double well and forming symmetric and antisymmetric combinations of the two lowest eigenstates, yielding a pair of maximally localized orbitals. Extracting  $(t, U)$  from  $(V, \gamma)$  ensures parameter consistency between the continuum simulation and any tight-binding reference, thereby enabling a controlled verification against the measurements in Ref. [26].

#### A. Single-particle tunneling

We first benchmark our numerics against the single-atom tunneling data reported in Figure S1 of Ref. [26]. In the experiment, single atoms are loaded into isolated double wells and initially pinned to one side by applying an energy offset. When this offset is reduced, the atom remains localized provided the short-lattice depth,  $V_S$ , is large (deep wells). Lowering  $V_S$  to a target value initiates Rabi-like tunnel oscillations, and the population in the left well is sampled at various hold times. The resulting trace is fitted to a sinusoid, from which an oscillation frequency is extracted. Throughout these measurements the long-lattice depth is fixed at

$$V_L = 36.5 E_r^{\text{long}}, \quad E_r^{\text{long}} = \frac{\hbar^2}{8m(2a_x)^2}. \quad (11)$$

The short-lattice depth is varied and throughout this work will be given in units of  $E_r^{\text{short}} = \frac{\hbar^2}{8ma_x^2}$ .

In the simulation we bypass the state-preparation sequence and start directly with the initial state being  $w_L(x)$ , at the desired lattice depths  $(V_S, V_L)$ . We then evolve  $\psi(x, \tau)$  in time using the single particle version of Eq. 2 and monitor the left-well population

$$P_L(\tau) = \int_{-\infty}^0 |\psi(x, \tau)|^2 dx. \quad (12)$$

As in the experiment,  $P_L(\tau)$  is fitted to a sinusoid,  $P_L(\tau) = A \cos(2\pi f \tau + \varphi) + C$ , and we identify  $2t/\hbar$  as the tunneling frequency.

In Figure 1 we present a comparison between the tunneling frequencies found in the experiment (red circles) and those calculated in our numerical simulations (black line). We find excellent quantitative agreement without parameter tuning: the maximal deviation is  $\sim 8\%$ , while the majority of points agree to within  $2\%$ . In addition, we calculated the tunneling frequency directly using Eq. 10, and obtained the same values observed in the numerics. This confirms that the continuum simulation faithfully reproduces the single-particle tunneling dynamics under the experimental conditions.

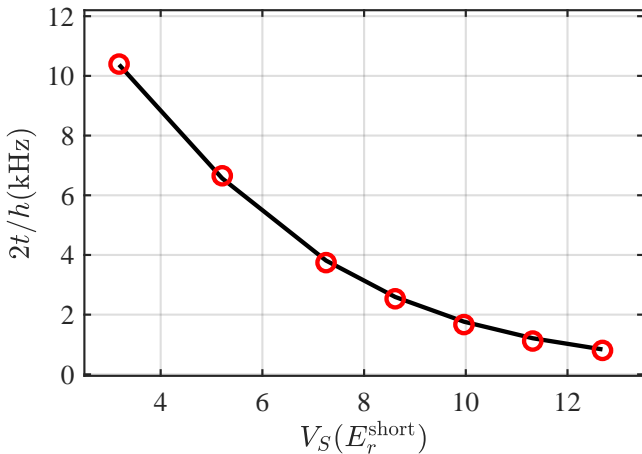


FIG. 1. **Single-particle tunneling: simulation versus experiment.** Tunneling frequency as a function of the short-lattice depth  $V_S$ . Simulation (solid black) compared with the experimental data (red circles) from Figure S1 of Ref. [26].

### B. Two-particle tunneling

As a second benchmark, we compare our results with the two-fermion measurements reported in Figure 3 of Ref. [26], which probe dynamics in the presence of repulsive interactions. Two experimental protocols are considered: (i) *spin-exchange*, where two atoms with opposite spins are initialized on *opposite* sites of a double well, and (ii) *pair-tunneling*, where both atoms start on the *same* site. The on-site interaction is tuned via a Feshbach resonance, and reported to be  $U = h \times 6.7$  kHz. The long-lattice depth is held fixed at  $V_L = 39.5 E_r^{\text{long}}$ . The short-lattice depth is linearly ramped from  $54 E_r^{\text{short}}$  down to  $5.54 E_r^{\text{short}}$  over  $500 \mu\text{s}$ , held for a variable duration  $\tau_h$ , and then ramped back up over another  $500 \mu\text{s}$ . The relevant occupations,  $P_{|\uparrow,\downarrow\rangle}$ , for spin exchange, and  $P_{|\uparrow\downarrow,0\rangle}$  for pair tunneling, are measured at the end of the full sequence.

In our simulations, we replicate the same ramp profiles and holding times, scanning  $\tau_h \in [0, 0.5]$  ms. Initial two-particle states are prepared either as opposite-spin fermions localized on different sites or co-localized on the same site. After time evolution, we project onto the site-occupation basis and record  $P_{|\uparrow,\downarrow\rangle}$  and  $P_{|\uparrow\downarrow,0\rangle}$  as functions of  $\tau_h$ , enabling a direct comparison with the experimental observables.

The key difference compared to the single-particle tunneling simulation is the inclusion of interparticle interactions. The contact-interaction coefficient  $\gamma$  is obtained from Eq. 9 for the double-well potential at the relevant double trap configurations, specifically  $(V_L, V_S) = (34.9 E_r^{\text{long}}, 5.54 E_r^{\text{short}})$  of spin-exchange, and  $(V_L, V_S) = (36.8 E_r^{\text{long}}, 6 E_r^{\text{short}})$  for pair tunneling. From the values of  $U$  given in [26] we deduce:  $\gamma/h = 4.756$  kHz  $\times \mu\text{m}$  and  $\gamma/h = 4.361$  kHz  $\times \mu\text{m}$ , for spin exchange and pair tunneling, respectively.

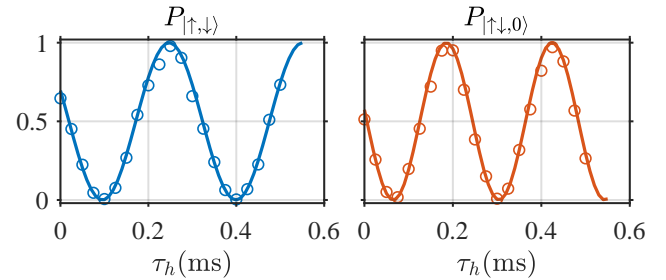


FIG. 2. **Simulation of spin-exchange (left) and pair-tunneling (right) oscillations** for several holding times  $\tau_h$ . The fit to a sinusoidal form is shown as well as a solid line.

We simulate both spin-exchange and pair-tunneling oscillations with these parameters, and results are presented in Figure 2. Fitting the site-occupation traces to a sinusoidal form yields exchange frequencies  $J/h = 3.324$  kHz for spin-exchange, and  $J/h = 4.182$  kHz for pair tunneling. In the spin-exchange case, the agreement with the experimental results of Ref. [26] is excellent: our fitted frequency exactly matches the reported  $3.32(3)$  kHz, and the extracted phase (i.e., the occupation at  $\tau_h = 0$ ) also coincides.

In the pair-tunneling regime, two discrepancies become apparent. First, the simulated oscillation frequency,  $4.182$  kHz, exceeds the measured  $3.8$  kHz of Ref. [26] by a noticeable margin. Second, the fitted phase of the sinusoid differs from the experimental trace. Since these differences arise only in the pair-tunneling regime, we attribute them to deviations of the real interatomic interaction from the idealized delta-function potential, or from slight inaccuracies in the initial conditions.

Figure 3 illustrates the time evolution of the absolute value of the pair-tunneling wavefunction,  $|\psi_{\uparrow\downarrow}(x_1, x_2, t)|$ , at several representative moments. Initially, the two-particle wavefunction is localized in the left well. Owing to the repulsive delta-function interaction, the amplitude is slightly distorted along the diagonal  $x_1 = x_2$  [Figure 3(a)]. As the barrier height is reduced, the pair begins to tunnel back and forth between wells, while part of the wavefunction separates, placing the two particles in opposite traps ( $|x_1 - x_2| > d/2$ ) [Figure 3(b–c)]. When the barrier is raised again, the wavefunction becomes more confined at each site, and the probability distribution of particle positions depends sensitively on the holding time  $\tau_h$  [Figure 3(d)].

In addition, we benchmarked the spin-exchange oscillations in the strongly interacting regime  $U/t \gg 1$ , where the exchange frequency is well approximated by  $J \simeq 4t^2/U$ . Figure 4 compares our simulations with the experimental data (Figure S2 in [26]), and shows very good agreement across the scanned parameters. Achieving quantitative consistency, however, requires rescaling the contact-interaction coefficient  $\gamma$  by a constant factor of 0.82.

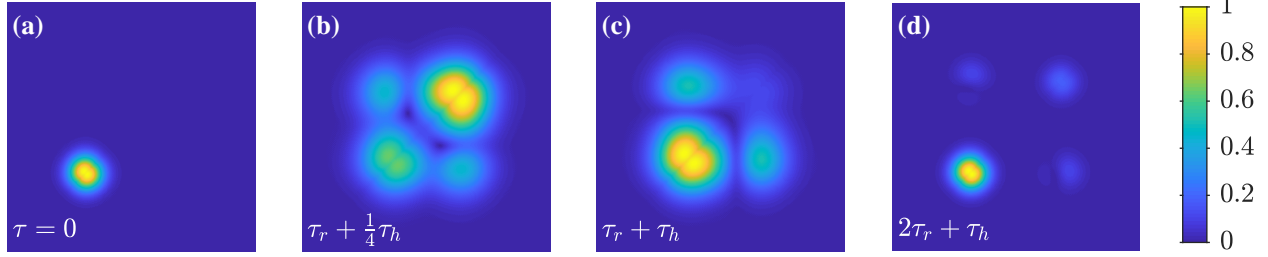


FIG. 3. **Pair tunneling waveform evolution.** Panels (a)-(d) depict the absolute value of the two-particle waveform,  $|\psi_{\uparrow\downarrow}(x_1, x_2, \tau)$ , for different times during the operation of the sequence.  $\tau_r = 0.5\text{ms}$  -the ramping time, and  $\tau_h = 0.2\text{ms}$  - the holding time.  $x_1$  and  $x_2$  are the horizontal and vertical axes, respectively (each is  $3\mu\text{m}$  wide).

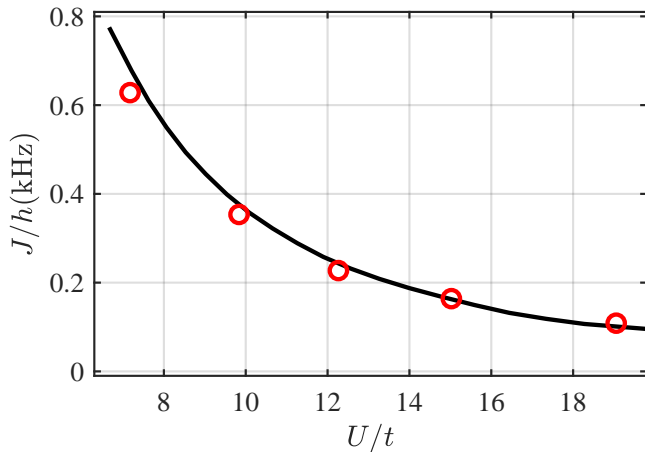


FIG. 4. **Spin-exchange oscillations – simulation versus experiment.** The tunneling frequency is extracted from a series of simulations in which the short-lattice depth  $V_S$  is varied while the interaction strength  $\gamma$  is kept fixed. The on-site interaction  $U$  is computed from Eq. 9; however, to quantitatively match the experimental data, it must be rescaled by a constant factor of 0.82. This rescaling yields the solid black curve, which shows excellent agreement with the experimental results (red circles) reported in Figure S2 of Ref. [26] and follows the expected scaling  $J = 4t^2/U$ .

### C. Tunneling-based $\sqrt{\text{SWAP}}$ gate sequences

A key result of Ref. [26] is the experimental implementation of a tunneling-based  $\sqrt{\text{SWAP}}$  gate. After establishing spin-exchange interactions, the authors proceed to realize two-qubit gates using controlled tunneling within the Fermi-Hubbard framework. The initial state consists of two atoms prepared in opposite wells,  $|\uparrow, \downarrow\rangle$ , separated by a high barrier ( $V_S = 54E_r^{\text{short}}$ ). To suppress unwanted pair-occupancy states ( $|\uparrow\downarrow, 0\rangle$  or  $|0, \uparrow\downarrow\rangle$ ), they introduce three strategies: (i) operate in the strong-interaction regime  $U/t \gg 1$ , where  $J \approx 4t^2/U$ , yielding

very slow gates; (ii) use fast ramps to increase and decrease the tunneling rate  $t$ , and fine-tune  $U/t$  to  $4/\sqrt{3}$ , at which point the spin and charge sectors become independent at times  $N \times h/(4J)$  (with  $N$  an integer); (iii) vary  $t$  slowly compared to  $U$ , but still faster than  $J$ , or employ smoothly shaped Blackman pulses to obtain intermediate gate speeds. Using the last approach, the authors report a fidelity of 99.75% for the Blackman-pulse sequence with a duration of 1.125 ms.

We follow the experimental protocols and, for strategy (ii), use the reported ramp duration of  $\tau_r = 50\mu\text{s}$  while setting  $V_L$  and  $V_s$  according to Table S2 of Ref. [26]. The hold time  $\tau_h$  and the interaction strength  $\gamma$  are then optimized to maximize the resulting gate fidelity. For strategy (iii), which uses a Blackman pulse, we similarly optimize both the pulse duration  $\tau_p$  and the interaction parameter  $\gamma$ .

For the fast-ramp sequence, the maximal fidelity obtained is 92.53%. The corresponding state populations are  $P_{|\uparrow, \downarrow\rangle} = 0.5614$  and  $P_{|\downarrow, \uparrow\rangle} = 0.3932$ , while the doublon population indeed remains below 5%, in agreement with the observations of Ref. [26]. The optimized hold time and interaction coefficient are  $\tau_h = 78.3\mu\text{s}$  and  $\gamma/h = 3.56\text{ kHz }\mu\text{m}$ , respectively. These values are close to the reported experimental parameters ( $74.7\mu\text{s}$  and  $3.92\text{ kHz }\mu\text{m}$ ). The corresponding waveform evolution, shown in Figure 5, exhibits sizeable excursions outside the lowest-band manifold during the ramp. This leakage explains why a minimal two-site Fermi-Hubbard description cannot reproduce the full dynamics of the fast-ramp protocol.

For the Blackman-pulse protocol, the maximal fidelity reaches 99.79%, in excellent agreement with the experimental value of 99.75(6)%. The populations are  $P_{|\uparrow, \downarrow\rangle} = 0.51$  and  $P_{|\downarrow, \uparrow\rangle} = 0.488$ . We find that the optimized pulse duration is  $\tau_p = 1.175\text{ ms}$ , very close to the experimentally reported value of 1.125 ms. However, the optimized interaction strength is found to be  $\gamma/h = 7.35\text{ kHz }\mu\text{m}$ , markedly different than the value reported in the experiment ( $4.84\text{ kHz }\mu\text{m}$ ). The corresponding evolution,

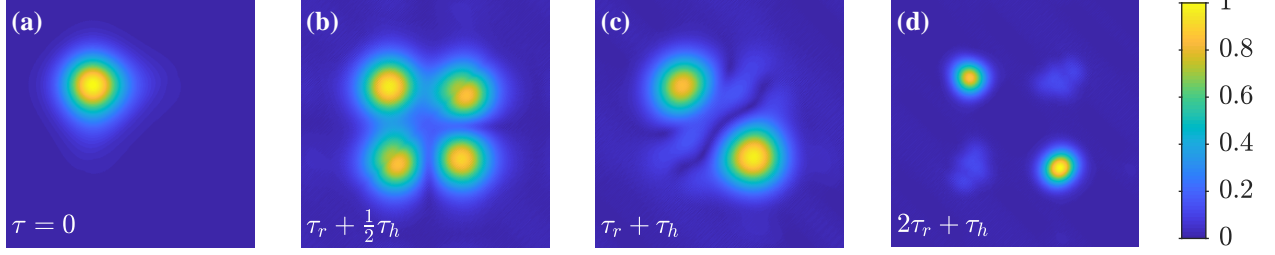


FIG. 5.  $\sqrt{\text{SWAP}}$  gate with fast ramping of amplitudes. Panels (a)-(d) depict the absolute value of the two-particle waveform distribution,  $|\psi_{\uparrow\downarrow}(x_1, x_2, \tau)|$ , for different times during the operation of the sequence, with  $x_1$  and  $x_2$  being the horizontal and vertical axes, respectively (each is  $3\mu\text{m}$  wide).

shown in Figure 6, is nearly adiabatic: the wavefunction remains confined to the desired low-energy subspace throughout the sequence, consistent with the smooth spectral characteristics of the Blackman envelope.

#### IV. FAST SWAP USING DYNAMIC CONTROL OF THE SUPERLATTICE

We now proceed to discuss our protocol for a fast  $\sqrt{\text{SWAP}}$  gate based on optimized, time-dependent control of the superlattice amplitudes  $V_L(\tau)$  and  $V_S(\tau)$ . As a first step, we optimize *single-particle* transfer from the left to the right well. With the interaction tuned to zero (e.g., via the magnetic field), this procedure realizes an effective SWAP operation for two particles through independent transport. Once this is accomplished, a  $\sqrt{\text{SWAP}}$  gate can be implemented by introducing back the interaction between the particles during the SWAP process [36].

To implement a SWAP gate, we numerically solve Eq. 2 in the single-particle sector (coordinate  $x$ ), using the superlattice potential  $V_{\text{ext}}(x, \tau)$  from Eq. 1. We restrict to experimentally convenient ranges  $V_L < 140 E_r^{\text{long}}$  and  $V_S < 50 E_r^{\text{short}}$ . A naive strategy, namely rapidly turning off the short lattice (ramp  $\sim 1\mu\text{s}$ ) while increasing the long lattice to its maximum, in the spirit of the added harmonic confinement in Sec. II, performs poorly here. The reason is that the residual long-lattice is appreciably anharmonic, which distorts the wave packet and limits the best achievable fidelity to  $\sim 92.4\%$  ( $\sim 85.4\%$ ) for a single- (two-) particle SWAP.

To mitigate the effect of anharmonicity, we instead ramp  $V_L$  *up* rapidly while lowering  $V_S$  *continuously* to (near) zero and subsequently restoring it, which preserves a quasi-harmonic confinement throughout the motion, as shown in Figure 7a. We use the following envelopes:

$$V_S(\tau) = \frac{V_S(0)}{\tau_{\text{gate}}^2} (2\tau - \tau_{\text{gate}})^2 \quad (13)$$

$$V_L(\tau) = V_L^{\text{max}} - \frac{V_L^{\text{max}} - V_L(0)}{\tau_{\text{gate}}^8} (2\tau - \tau_{\text{gate}})^8, \quad (14)$$

with  $V_L^{\text{max}} = 140$ ,  $V_L(0) = 20$ ,  $V_S(0) = 45.93$  (in units of  $E_r^{\text{long}}$  and  $E_r^{\text{short}}$ , respectively), and  $\tau_{\text{gate}} = 21.26\mu\text{s}$ . The resulting total potential is depicted in Figure 7b.

With these parameters we achieve a transfer fidelity of  $\sim 99.97\%$  and  $\sim 99.94\%$  for the single- and two-particle SWAP, respectively. Figure 7c depicts the corresponding dynamics: the wave packet travels swiftly from the left well to the central region and is subsequently recaptured in the right well, while remaining spectrally narrow and avoiding significant leakage to higher bands.

#### V. FAST $\sqrt{\text{SWAP}}$ GATE

Building on the single-particle transfer of Sec. IV, implementing a  $\sqrt{\text{SWAP}}$  becomes straightforward: we solve the full two-particle Schrödinger equation (Eq. 2) with the superlattice potential  $V_{\text{ext}}(x, \tau)$  of Eq. 1, driven by the optimized envelopes  $V_L(\tau)$  and  $V_S(\tau)$ . The contact interaction is set by a single magnetic-field value  $\gamma$  that is *held constant* throughout the pulse. We then optimize over a small set of control parameters ( $V_L(0)$ ,  $V_S(0)$ ,  $\tau_{\text{gate}}$  and  $\gamma$ ) to maximize the gate fidelity.

With this protocol we obtain a best fidelity of 99% using the following parameters:

$$\begin{aligned} V_L^{\text{max}} &= 140 E_r^{\text{long}} \\ V_L(0) &= 20 E_r^{\text{long}} \\ V_S(0) &= 41.35 E_r^{\text{short}} \\ \tau_{\text{gate}} &= 21.2 \mu\text{s} \\ \gamma/h &= 30.96 \text{ kHz} \times \mu\text{m} \end{aligned} \quad (15)$$

While the peak fidelity is somewhat below that of the Blackman tunneling sequence, the present gate is substantially *faster*: the duration is shorter by a factor of  $\sim 54$  relative to the Blackman protocol, and by  $\sim 8.4$

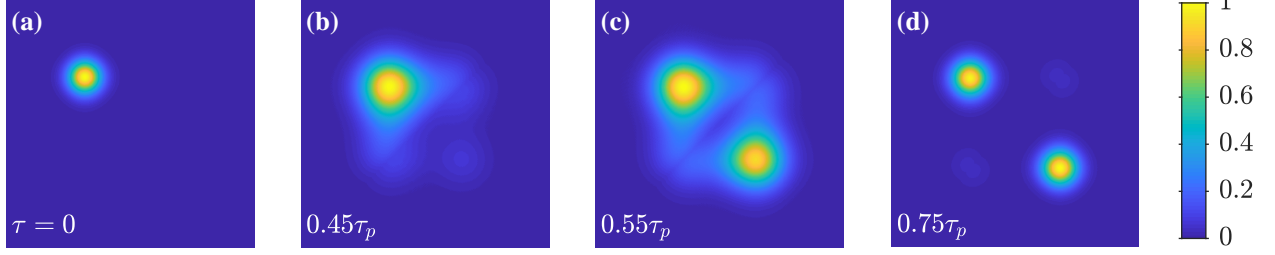


FIG. 6.  $\sqrt{\text{SWAP}}$  gate via Blackman pulse. Panels (a)-(d) depict the absolute value of the two-particle probability distribution,  $|\psi_{\uparrow\downarrow}(x_1, x_2, \tau)|$ , for different times during the operation of the sequence, with  $x_1$  and  $x_2$  being the horizontal and vertical axes, respectively (each is  $3\mu\text{m}$  wide).

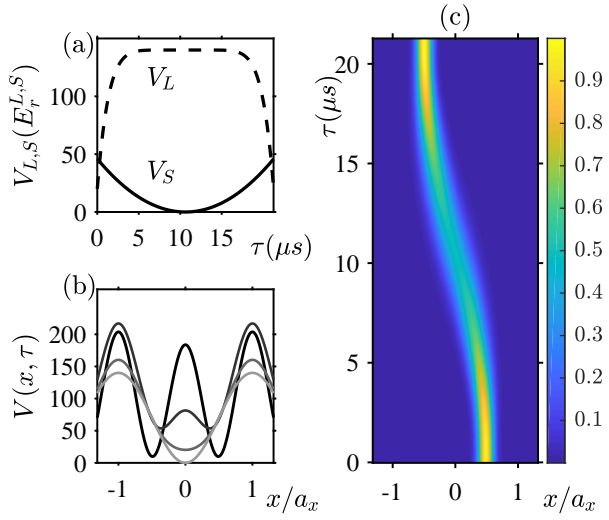


FIG. 7. Fast single-particle transfer for a SWAP. (a) Optimized envelopes for the short- and long-lattice depths,  $V_S(\tau)$  and  $V_L(\tau)$ , over the gate duration  $\tau_{\text{gate}}$ . (b) Double-well potential snapshots every  $\tau_{\text{gate}}/6$ , from  $\tau = 0$  (black) to  $\tau = 0.5 \tau_{\text{gate}}$  (light gray). (c) Single-particle probability density  $|\psi(x, \tau)|^2$  (normalized to its maximum), illustrating the wave-packet transport from the left to the right well.

compared with a fast-ramp implementation (while still delivering much higher fidelity than the latter). As expected, the required interaction strength here is larger, by about a factor of six.

Figure 8 illustrates the two-particle dynamics during the pulse sequence. The joint wave packet moves toward the central region, where interaction-induced phase accumulation and exchange generate entanglement; the wave-packet components then separate and are recaptured in distinct wells at the end of the sequence. It is instructive to compare these dynamics with those of the Blackman gate shown in Figure 6. A key qualitative difference is the appearance of cross-diagonal stripe pat-

terns in the former, which are absent in the latter. These stripes arise from the interference between incoming and reflected wave packets and constitute a clear signature of a collisional process [36], whereas the dynamics in Figure 6 is dominated by tunneling.

Further improvement to the fidelity is possible if a larger superlattice depth is available. For example, increasing the ceiling to  $V_L^{\text{max}} = 700E_r^{\text{long}}$  allows an optimized fidelity of 99.41% with a shorter gate time  $\tau_{\text{gate}} = 9.2 \mu\text{s}$ . This shorter gate requires a stronger contact interaction,  $\gamma/h = 63 \text{ kHz} \times \mu\text{m}$ .

These trends are consistent with the intuition from our previous work [36]: higher effective confinement (i.e., stronger mid-pulse focusing) enhances the fidelity. A convenient proxy is a pseudo-squeezing parameter,

$$r = \ln \left[ \sigma_0 / \sigma \left( \frac{1}{2} \tau_{\text{gate}} \right) \right],$$

defined by the ratio of the wave-packet width at the start ( $\sigma_0$ ) and at mid-gate. We find  $r = -0.688$  for  $V_L^{\text{max}} = 140$  and  $r = -0.629$  for  $V_L^{\text{max}} = 700$ , in line with the observed fidelity gains as the mid-sequence confinement is strengthened.

*Robustness to lattice-amplitude variations* - In typical superlattice experiments, spatial intensity inhomogeneities of the lattice beams produce site-to-site depth variations at the  $\sim 5\%$  level [38]. Even a uniform rescaling of the control envelopes,  $V_{L/S}(\tau) \rightarrow (1 \pm 0.05) V_{L/S}(\tau)$ , degrades performance because the fixed timing no longer matches the effective tunneling rates. In our simulations, the single-pulse  $\sqrt{\text{SWAP}}$  fidelity decreases from 99% to  $\approx 97.5\%$  under a  $\pm 5\%$  global scale change.

To mitigate this sensitivity, and to slightly increase the overall fidelity, we propose implementing the gate  $\text{SWAP}^{3/4}$  and repeating it twice, thereby realizing the maximally entangling gate  $\text{SWAP}^{3/2}$  (which is equivalent to  $\text{SWAP} \circ \sqrt{\text{SWAP}}$ ). The improved fidelity of  $\text{SWAP}^{3/2}$  relative to  $\sqrt{\text{SWAP}}$  originates from two main effects. First, the required contact interaction strength is substantially reduced (by approximately 60%), which

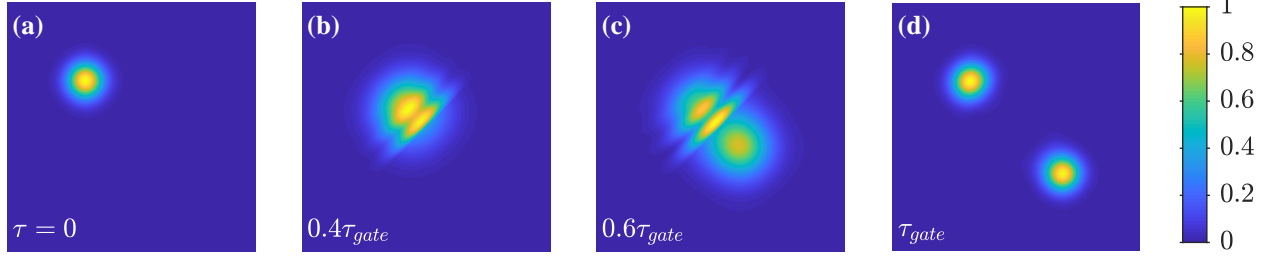


FIG. 8.  $\sqrt{\text{SWAP}}$  gate via fast dynamic control. Panels (a)-(d) depict the two-particle probability distribution,  $|\psi_{\uparrow\downarrow}(x_1, x_2, \tau)|$ , for different times during the operation of the sequence, with  $x_1$  and  $x_2$  being the horizontal and vertical axes, respectively (each is  $3\mu\text{m}$  wide).  $\tau_{\text{gate}} = 21.2\mu\text{s}$

directly suppresses interaction-induced errors. The reduced sensitivity to amplitude variations arises from the approximate time-reversal symmetry of the repeated sequence: errors accumulated during the first application are partially canceled during the second. As a result, the double-SWAP $^{3/4}$  protocol yields higher fidelities than a single SWAP $^{3/4}$  gate in the presence of amplitude fluctuations.

With these modifications, and after optimizing both the lattice amplitudes and interaction strength, we obtain a fidelity of 99.3% for the SWAP $^{3/4}$  gate and 99.17% for the composite SWAP $^{3/2}$  gate. Importantly, under lattice-amplitude variations of up to  $\pm 5\%$ , the fidelity remains above 98.7%. A representative robust operating point is given by

$$\begin{aligned} V_L^{\max} &= 140E_r^{\text{long}} \\ V_L(0) &= 20E_r^{\text{long}} \\ V_S(0) &= 43.4E_r^{\text{short}} \\ \tau_{\text{gate}} &= 2 \times 21.39 \mu\text{s} \\ \gamma/h &= 12.8 \text{ kHz} \times \mu\text{m} . \end{aligned} \quad (16)$$

## VI. DISCUSSION

We have introduced an optimized sequence for implementing a  $\sqrt{\text{SWAP}}$  gate on a superlattice platform. This approach extends our previous work [36], in which two atoms were driven to interact within a central, ideal har-

monic trap. In contrast, the present method relies solely on experimentally accessible control parameters of a superlattice. Since it does not require an additional external potential, it is much easier to implement in existing experiments.

Our results demonstrate that carefully timed modulation of the superlattice amplitudes enables coherent swapping of atoms between opposite lattice sites. When interatomic interactions are included, this mechanism naturally realizes a  $\sqrt{\text{SWAP}}$  gate. The performance of the proposed protocol was investigated numerically using a model that goes beyond the tight-binding Fermi–Hubbard approximation. To validate our simulation framework, we benchmarked it against the experimental results reported in [26], finding excellent agreement, although our simulations were performed in one dimension. This correspondence strongly indicates that the proposed sequence can be implemented in realistic three-dimensional superlattices.

Finally, our numerical analysis shows that the gate exhibits high robustness, achieving fidelities exceeding 99%. A key advantage of this protocol is its remarkably short operation time, on the order of  $20\mu\text{s}$ , which is roughly two orders of magnitude faster than tunneling-based gates (typically  $\sim 1\text{ms}$ ) [26].

## ACKNOWLEDGMENTS

This research was supported by the Pazy Research Foundation and by the Helen Diller Quantum Center.

**Note added.** While finalizing this manuscript, we became aware of a closely related recent work [42].

---

[1] A. Lucas, “Ising formulations of many np problems,” *Frontiers in Physics* **2**, 5 (2014).  
[2] D. J Egger, J. Mareček, and S Woerner, “Warm-starting quantum optimization,” *Quantum* **5**, 479 (2021).  
[3] G. Buonaiuto, F. Gargiulo, G. De Pietro, M. Esposito, and M. Pota, “Best practices for portfolio optimization

by quantum computing, experimented on real quantum devices," *Scientific Reports* **13**, 19434 (2023).

[4] P. W. Shor, "Polynomial-time algorithms for prime factorization and discrete logarithms on a quantum computer," *SIAM Journal on Computing* **26**, 1484 (1997).

[5] D. J. Bernstein, J. Buchmann, and E. Dahmen, eds., *Post-Quantum Cryptography* (Springer, 2009).

[6] A. Aspuru-Guzik, A. D. Dutoi, P. J. Love, and M. Head-Gordon, "Simulated quantum computation of molecular energies," *Science* **309**, 1704 (2005).

[7] S. McArdle, S. Endo, A. Aspuru-Guzik, S. C. Benjamin, and X. Yuan, "Quantum computational chemistry," *Reviews of Modern Physics* **92**, 015003 (2020).

[8] L. Clinton, T. Cubitt, B. Flynn, F. M. Gambetta, J. Klassen, A. Montanaro, S. Piddock, R. A. Santos, and E. Sheridan, "Towards near-term quantum simulation of materials," *Nature Communications* **15**, 211 (2024).

[9] J. Biamonte, P. Wittek, N. Pancotti, P. Rebentrost, N. Wiebe, and S. Lloyd, "Quantum machine learning," *Nature* **549**, 195 (2017).

[10] A. Melnikov, M. Kordzanganeh, A. Alodjants, and R. K. Lee, "Quantum machine learning: from physics to software engineering," *Advances in Physics: X* **8**, 2165452 (2023).

[11] D. Peral-García, J. Cruz-Benito, and F. J. García-Péñalvo, "Systematic literature review: Quantum machine learning and its applications," *Computer Science Review* **51**, 100619 (2024).

[12] S. B. Bravyi and A. Y. Kitaev, "Fermionic quantum computation," *Annals of Physics* **298**, 210 (2002).

[13] D. González-Cuadra, D. Bluvstein, M. Kalinowski, R. Kaubruegger, N. Maskara, P. Naldesi, T.V. Zache, A.M. Kaufman, M.D. Lukin, H. Pichler, B. Vermersch, J. Ye, and P. Zoller, "Fermionic quantum processing with programmable neutral atom arrays," *Proceedings of the National Academy of Sciences* **120**, e2304294120 (2023).

[14] R. Babbush, W. J. Huggins, D. W. Berry, S. F. Ung, A. Zhao, D. R. Reichman, H. Neven, and J. Lee, "Quantum simulation of exact electron dynamics can be more efficient than classical mean-field methods," *Nature Communications* **14**, 4058 (2023).

[15] J. T. Seeley, M. J. Richard, and P. J. Love, "The bravyi–kitaev transformation for quantum computation of electronic structure," *Journal of Chemical Physics* **137**, 224109 (2012).

[16] I. Bloch, J. Dalibard, and W. Zwerger, "Many-body physics with ultracold gases," *Reviews of Modern Physics* **80**, 885–964 (2008).

[17] D. Bluvstein, H. Levine, G. Semeghini, T. T. Wang, S. Ebadi, M. Kalinowski, A. Keesling, N. Maskara, H. Pichler, Greiner, M, V. Vuletić, and M. D. Lukin, "A quantum processor based on coherent transport of entangled atom arrays," *Nature* **606**, 269 (2022).

[18] H. J. Manetsch, G. Nomura, E. Bataille, K. H. Leung, and M. Endres, "A tweezer array with 6100 highly coherent atomic qubits," *Nature* **647**, 60 (2025).

[19] S. Kotochigova, "Neutral atoms in optical tweezers as messenger qubits for scaling up a trapped ion quantum computer," *Physical Review Research* **7**, 033212 (2025).

[20] M. Endres, "Quantum science with optical tweezer arrays of ultracold atoms and molecules," *Nature Physics* **17**, 1324 (2021).

[21] L. Pause, L. Sturm, M. Mittenbühler, S. Amann, T. Preuschoff, D. Schäffner, and G. Birkl, "Supercharged two-dimensional tweezer array with more than 1000 atomic qubits," *Optica* **11**, 222 (2024).

[22] A. J. Park, J. Trautmann, N. Šantić, V. Klüsener, A. Heinz, I. Bloch, and S. Blatt, "Cavity-enhanced optical lattices for scaling neutral atom quantum technologies to higher qubit numbers," *PRX Quantum* **3**, 030314 (2022).

[23] R. Tao, M. Ammenwerth, F. Gyger, I. Bloch, and J. Zeiher, "High-fidelity detection of large-scale atom arrays in an optical lattice," *Physical Review Letters* **133**, 013401 (2024).

[24] M. A. Norcia, H. Kim, W. B. Cairncross, M. Stone, A. Ryou, M. Jaffe, M. O. Brown, K. Barnes, P. Battaglino, T. C. Bohdanowicz, A. Brown, K. Cassella, C.-A. Chen, R. Coxe, D. Crow, J. Epstein, C. Griger, E. Halperin, F. Hummel, A. M. W. Jones, J. M. Kindem, J. King, K. Kotru, J. Lauigan, M. Li, M. Lu, E. Megidish, J. Marjanovic, M. McDonald, T. Mittiga, J. A. Muniz, S. Narayanaswami, C. Nishiguchi, T. Paule, K. A. Pawlak, L. S. Peng, K. L. Pudenz, D. Rodríguez Pérez, A. Smull, D. Stack, M. Urbanek, R. J. M. van de Veedonk, Z. Vendeiro, L. Wadleigh, T. Wilkason, T.-Y. Wu, X. Xie, E. Zalys-Geller, X. Zhang, and B. J. Bloom, "Iterative assembly of atom arrays with cavity-enhanced optical lattices," *PRX Quantum* **5**, 030316 (2024).

[25] F. Gyger, M. Ammenwerth, R. Tao, H. Timme, S. Snigirev, I. Bloch, and J. Zeiher, "Continuous operation of large-scale atom arrays in optical lattices," *Physical Review Research* (2024).

[26] P. Bojović, T. Hilker, S. Wang, J. Obermeyer, M. Barendregt, D. Tell, T. Chalopin, P. M. Preiss, I. Bloch, and T. Franz, "High-fidelity collisional quantum gates with fermionic atoms," (2025), arXiv:2506.14711 [cond-mat.quant-gas].

[27] T. Wilk, A. Gaëtan, C. Evellin, J. Wolters, Y. Miroshnychenko, P. Grangier, and A. Browaeys, "Entanglement of two individual neutral atoms using rydberg blockade," *Physical Review Letters* **104**, 010502 (2010).

[28] L. Isenhower, E. Urban, X. L. Zhang, A. T. Gill, T. Henage, T. A. Johnson, T. G. Walker, and M. Saffman, "Demonstration of a neutral atom controlled-not quantum gate," *Physical Review Letters* **104**, 010503 (2010).

[29] A.G. Radnaev, W.C. Chung, D.C. Cole, D. Mason, T.G. Ballance, M.J. Bedalov, D.A. Belknap, M.R. Berman, M. Blakely, I.L. Bloomfield, P.D. Buttler, C. Campbell, A. Chopinaud, E. Copenhagen, M.K. Dawes, S.Y. Eu-banks, A.J. Friss, D.M. Garcia, J. Gilbert, M. Gillette, P. Goiporia, P. Gokhale, J. Goldwin, D. Goodwin, T.M. Graham, C.J. Guttormsson, G.T. Hickman, L. Hurtley, M. Iliev, E.B. Jones, R.A. Jones, K.W. Kuper, T.B. Lewis, M.T. Lichtman, F. Majdeteimouri, J.J. Mason, J.K. McMaster, J.A. Miles, P.T. Mitchell, J.D. Murphree, N.A. Neff-Mallon, T. Oh, V. Omole, C. Parlo Simon, N. Pederson, M.A. Perlin, A. Reiter, R. Rines, P. Romlow, A.M. Scott, D. Stieffvater, J.R. Tanner, A.K. Tucker, I.V. Vinogradov, M.L. Warter, M. Yeo, M. Saffman, and T.W. Noel, "Universal neutral-atom quantum computer with individual optical addressing and nondestructive readout," *PRX Quantum* **6**, 030334 (2025).

[30] R. Finkelstein, R. B. Tsai, X. Sun, P. Scholl, S. Direkci, T. Gefen, J. Choi, A. L. Shaw, and M. Endres, "Universal quantum operations and ancilla-based read-out for

tweezer clocks,” *Nature* **634**, 321 (2024).

[31] O. Mandel, M. Greiner, A. Widera, T. Rom, T. W. Hänsch, and I. Bloch, “Controlled collisions for multi-particle entanglement of optically trapped atoms,” *Nature* **425**, 937 (2003).

[32] S. Fölling, S. Trotzky, P. Cheinet, M. Feld, R. Saers, A. Widera, T. Müller, and I. Bloch, “Direct observation of second-order atom tunnelling,” *Nature* **448**, 1029 (2007).

[33] M. Anderlini, P. J. Lee, B. L. Brown, J. Sebby-Strabley, W. D. Phillips, and J. V. Porto, “Controlled exchange interaction between pairs of neutral atoms in an optical lattice,” *Nature* **448**, 452 (2007).

[34] S. Trotzky, P. Cheinet, S. Fölling, M. Feld, U. Schnorrberger, A. M. Rey, A. Polkovnikov, E. A. Demler, M. D. Lukin, and I. Bloch, “Time-resolved observation and control of superexchange interactions with ultracold atoms in optical lattices,” *Science* **319**, 295 (2008).

[35] W.-Y. Zhang, M. Zhou, Y.-B. Tang, S. Wu, S.-C. Ji, and J.-W. Pan, “Scalable multipartite entanglement created by spin exchange in an optical lattice,” *Physical Review Letters* **131**, 073401 (2023).

[36] J. Nemirovsky and Y. Sagi, “Fast universal two-qubit gate for neutral fermionic atoms in optical tweezers,” *Physical Review Research* **3**, 013113 (2021).

[37] D. Hayes, P. S. Julienne, and I. H. Deutsch, “Quantum logic via the exchange blockade in ultracold collisions,” *Physical Review Letters* **98**, 070501 (2007).

[38] T. Chalopin, P. Bojović, D. Bourgund, S. Wang, T. Franz, I. Bloch, and T. A. Hilker, “Optical superlattice for engineering hubbard couplings in quantum simulation,” *Physical Review Letters* **134**, 053402 (2025).

[39] T. Busch, B. G. Englert, K. Rzażewski, and M. Wilkens, “Two cold atoms in a harmonic trap,” *Foundations of Physics* **28**, 549 (1998).

[40] C. Chin, R. Grimm, P. Julienne, and E. Tiesinga, “Feshbach resonances in ultracold gases,” *Reviews of Modern Physics* **82**, 1225 (2010).

[41] L. Thylen, “The beam propagation method: an analysis of its applicability,” *Optical and quantum electronics* **15**, 433 (1983).

[42] J. A. P. Reuter, J. Singh, T. Calarco, F. F. Motzoi, and R. Zeier, “Optimizing two-qubit gates for ultracold fermions in optical lattices,” (2025), arXiv:2512.03647 [cond-mat.quant-gas].